# Comparison of the Manganese Cluster in Oxygen-Evolving Photosystem II with Distorted Cubane Manganese Compounds through X-ray Absorption Spectroscopy

**Roehl M. Cinco[†,‡], Annette Rompel[†,‡,§], Hendrik Visser[†,‡], Guillem Aromí[⊥], George Christou[*,⊥], Kenneth Sauer[*,†,‡], Melvin P. Klein[*,‡], and Vittal K. Yachandra[*,‡]**

Melvin Calvin Laboratory, Physical Biosciences Division, Lawrence Berkeley National Laboratory, Berkeley, California 94720-5230, Department of Chemistry, University of California, Berkeley, California 94720-5230, and Department of Chemistry, Indiana University, Bloomington, Indiana 47405

[†] University of California.

[‡] Lawrence Berkeley National Laboratory.

[⊥] Indiana University.

## Abstract

X-ray absorption spectroscopy has been employed to assess the degree of similarity between the oxygen-evolving complex (OEC) in photosystem II (PS II) and a family of synthetic manganese complexes containing the distorted cubane $[Mn_4O_3X]$ core (X = benzoate, acetate, methoxide, hydroxide, azide, fluoride, chloride, or bromide). These $[Mn_4(\mu_3\text{-O})_3(\mu_3\text{-X})]$ cubanes possess $C_{3v}$ symmetry except for the X = benzoate species, which is slightly more distorted with only $C_s$ symmetry. In addition, $Mn_4O_3Cl$ complexes containing three or six terminal Cl ligands at three of the Mn were included in this study. The Mn K-edge X-ray absorption near edge structure (XANES) from the oxygen-ligated complexes begin to resemble general features of the PS II ($S_1$ state) spectrum, although the second derivatives are distinct from those in PS II. The extended X-ray absorption fine structure (EXAFS) of these Mn compounds also displays superficial resemblance to that of PS II, but major differences emerge on closer examination of the phases and amplitudes. The most obvious distinction is the smaller magnitude of the Fourier transform (FT) of the PS II EXAFS compared to the FTs from the distorted cubanes. Curve fitting of the Mn EXAFS spectra verifies the known core structures of the Mn cubanes, and shows that the number of the crucial 2.7 and 3.3 Å Mn–Mn distances differs from that observed in the OEC. The EXAFS method detects small changes in the core structures as X is varied in this series, and serves to exclude the distorted cubane of $C_{3v}$ symmetry as a topological model for the Mn catalytic cluster of the OEC. Instead, the method shows that even more distortion of the cubane framework, altering the ratio of the Mn–Mn distances, is required to resemble the Mn cluster in PS II.

---

[*] To whom correspondence should be addressed. Phone: (510) 486-4330. Fax: (510) 486-6059. vkyachandra@lbl.gov (V.K.Y.), christou@indiana.edu (G.C.), khsauer@lbl.gov (K.S.), or mpklein@lbl.gov (M.P.K.)..
[§]Present address: Institut für Biochemie, Westfälische Wilhelms-Universität, Wilhelm-Klemm-Strasse 2, 48149 Münster, Germany.

**Note Added in Proof.** More recent studies in our lab have re-examined the Mn K-edges from flash-induced S-states of PS II and the values for the IPEs (Robblee, J. H.; Messinger, J. et al., manuscript in preparation). The newer values for the edge positions are slightly different from those mentioned here, but the conclusions reached in the present comparison and in ref 18 remain unchanged.

**Supporting Information Available:** Parameters for forward Fourier transforms and Fourier filtering (Table 1S) and the raw $k^3$-weighted EXAFS spectra of the Mn cubanes and PS II (Figure 1S). This material is available free of charge via the Internet at http://pubs.acs.org.

## Introduction

One important goal of bioinorganic chemistry is to produce biomimetic systems that emulate existing active site metal centers structurally and, if possible, functionally. A tetranuclear manganese metalloenzyme under sustained study is the oxygen-evolving complex (OEC) of photosystem II (PS II).[1–4] The OEC forms an integral part of the photosynthetic energy transduction chain in green plants, algae, and cyanobacteria. The light-driven reaction of photosynthesis converts water and carbon dioxide into carbohydrates and dioxygen. The reducing equivalents for carbon fixation are provided by the OEC, which catalyzes the four-electron oxidation of water. These four electrons are transferred to the reaction center $P_{680}$ (via a redox-active tyrosine $Y_Z$) as the OEC cycles through five intermediate states $S_n$ ($n = 0$–4), gradually storing (up to 4) oxidizing equivalents.[5]

Although it has been the subject of ongoing bioinorganic synthesis and biochemical and biophysical studies, the exact structure of the photosynthetic Mn complex and the mechanism of water oxidation remain unknown. Nevertheless, X-ray absorption spectroscopy (XAS) and electron paramagnetic resonance (EPR) have provided insights into the structure and mechanism of the OEC.[6–8] Mn K-edge extended X-ray absorption fine structure (EXAFS) studies have shown the presence of at least two Mn–Mn pairs at ~2.7 Å, characteristic of di-$\mu$-oxo-bridged Mn, along with mostly oxygen ligation at 1.8–1.9 Å.[9] The Mn EXAFS also shows a longer distance interaction at ~3.3 Å, whose interpretations in the literature differ. It has been assigned to (1) one Mn–Mn and Mn–Ca at ~3.3 Å,[9–11] (2) one Mn–Mn at 3.3 Å,[12–14] (3) Mn–Mn or Mn–Ca,[15] or (4) Mn–Ca at 3.7 Å.[16] Further support for including a Mn–Ca at ~3.4 Å comes from recent strontium EXAFS studies.[17]

The Mn K-edge X-ray absorption near edge structure (XANES) has been used to probe the Mn valence at the different S states.[12,14–16,18–21] The Mn K-edge positions for the $S_0$, $S_1$, and $S_2$ states have been determined as inflection-point energies from second-derivative zero crossings,[22] and the overall edge shape is consistent with oxygen ligation.[9] The shifts in edge position along with characteristic changes in the edge shapes are indicative of Mn oxidation, so that the proposed Mn oxidation state assignments are as follows: $S_0$ (II, III, IV, IV) or (III, III, III, IV), $S_1$ (III, III, IV, IV), and $S_2$ (III, IV, IV, IV).

Chloride is, along with calcium, an essential cofactor for oxygen evolution.[23–25] Although $Cl^-$ can be replaced with $Br^-$ with retention of activity,[26] the role of this halide is still unknown. Until recently, Mn XAS methods have been inconclusive in finding the presence of halide in the ligation sphere of the Mn,[27,28] probably due to the low levels of $Cl^-$ ligation (one Cl atom per four Mn atoms). A recent report of polarized Mn EXAFS on oriented PS II membranes has implicated chloride as a ligand to the Mn cluster in the $S_3$ state.[29] The perturbation of the Mn–Mn 2.7 Å distance by fluoride ($F^-$, an inhibitor of oxygen activity) is the most direct evidence available of halide binding.[30]

Interest in the OEC and other Mn-containing metalloenzymes has stimulated the synthesis and characterization of polynuclear manganese complexes as possible structural (if not yet functional) models of the catalytic active site.[31–36] The class of proposed structure of the OEC at the various S states ($S_0$–$S_4$) has profound implications for the proposed mechanism for water oxidation. Mechanisms have been proposed based on the "dimerof-dimers" motif,[4,34,37] the "cubane" geometry,[38] and the "butterfly" cluster.[39] To sort through the multitude of possible models for the active site, the Mn EXAFS data from several multinuclear Mn model complexes have been analyzed and compared with the data from the OEC.[27,40,41] Earlier studies have shown that the symmetric cubane-like or butterfly motifs are incompatible with the observed numbers of 2.7 and 3.3 Å Mn–Mn vectors.[11,27] "Vector" here is defined as a pair of absorber and back-scatterer atoms that are not necessarily

bonded. The symmetric cubane was also ruled inconsistent on the basis of the dichroism observed for the EXAFS data from PS II.[42,43] From the many ways to arrange four Mn atoms to include distances of 2.7 and 3.3 Å consistent with the PS II EXAFS, 10 possibilities were considered in a previous study.[11] These are shown in Figure 1 and are grouped roughly as dimer-ofdimers (**1–4**), "trimer–monomer" (**5–7**) and "tetranuclear" (**8–10**) clusters.[11] Because of the presence of the requisite 1.8 Å Mn–O, 2.7 Å Mn–Mn, and ~3.3 Å Mn–Mn distances, any of these 10 topologies could be a viable model on the basis of XAS data. However, 4 of the 10 complexes (**1**, **5**, **6**, **7**) are particularly consistent with the coordination numbers predicted from PS II EXAFS, so that we currently favor the dimer-ofdimers cluster (especially **1** in Figure 1).[4,44]

One of the 10 possibilities, the $[Mn_4O_3]$ trigonal pyramid unit (**8**), is the subject of this current study, where we investigate a series of $[Mn_4(\mu_3\text{-}O)_3(\mu_3\text{-}X)]^{6+}$ units with Mn K-edge EXAFS and XANES, and compare them to recent data from the OEC. These compounds are of great interest because they satisfy the requisites for modeling the OEC active site: ~2.7 and ~3.3 Å Mn–Mn vectors, and (for many of the cubanes) mostly O ligands. These synthetic complexes are best described as "tetra-face-capped $Mn_4$ trigonal prisms" or, for convenience, highly distorted cubanes.[45] The central core consists of a $Mn_4$ pyramid with the $Mn^{IV}$ at the apex, three $Mn^{III}$ on the basal plane, a $\mu_3$-X bridging the basal plane, and a $\mu_3$-O bridging each of the remaining faces (Figure 2). Bridging carboxylate and terminal ligands complete the ligation of each Mn. In the following discussion the "core structure" is defined as the Mn cubane framework, along with the nearest-neighbor ligands to Mn. The core contains $Mn^{III}$–$Mn^{IV}$ and $Mn^{III}$–$Mn^{III}$ distances of ~2.8 and ~3.3 Å, respectively, which emphasize the severe deviation from true cubane ($T_d$) symmetry. The series of $[Mn_4O_3X(OAc)_3(dbm)_3]$ (dbmH = dibenzoylmethane) complexes have different X "substituents": X = **OAc**,[46]**OMe**,[47]**OH**,[47]**N$_3$**,[48,49]**Cl**,[45,50] and **Br**.[45] Closely related to this series is $[Mn_4O_3(OBz)(OBz)_3(dbm)_3]$, with X = **OBz** (benzoate, $O_2CPh$), and OBz bridges instead of OAc.[51] Included for comparison are the complexes $Mn_4O_3$**Cl$_4$**$(OAc)_3(py)_3$[48,52] and $(pyH)_3[Mn_4O_3$**Cl$_7$**$(OAc)_3]$[45] possessing single or double, respectively, Cl terminal ligation at the three $Mn^{III}$ atoms (Figure 2). Except for the **OBz** cubane core, which has virtual $C_s$ symmetry, the distorted cubanes have virtual $C_{3v}$ symmetry.

The goal of this study is to narrow the topological possibilities for the structure of the OEC by comparing the EXAFS and XANES data from this series of distorted cubane complexes $[Mn_4O_3X]$ of $C_{3v}$ symmetry to those from PS II. The $S_1$ state of PS II is chosen for comparison because this dark-stable resting state of the enzyme is the most characterized and accessible.[9,53] Because it probes the local structure of the $Mn_4O_3X$ core, EXAFS will be used to detect ligation changes in the series of complexes as the substituent X is altered. Of particular interest will be the substitution of Cl⁻ by Br⁻ or F⁻ to probe the effect of halide on the EXAFS of these complexes. The results of this comprehensive comparison indicate that, while the distorted cubanes do simulate some important features of the Mn EXAFS and XANES, major differences remain in the phases and amplitudes of the $k$-space EXAFS and the Fourier transforms (FTs). On the basis of these findings, the highly distorted cubane of $C_{3v}$ symmetry can be excluded as a topological analogue for the active site of the OEC, and a significantly greater distortion of the cubane core would be necessary to approach the observed OEC data. The EXAFS method can indeed detect the small changes in the core structures of these cubanes and can differentiate this type of tetranuclear Mn cluster from that present in PS II.

# Experimental Section

## Sample Preparation

The following tetranuclear Mn cubane complexes have been prepared and characterized: $[Mn_4O_3X(OAc)_3(dbm)_3]$ with X = **OAc**,[46]**OMe**,[47]**OH**,[47]**N_3**,[48]**F**,[49]**Cl**,[45,50]**Br**,[45] and **OBz** (with OAc replaced by OBz),[51] $Mn_4O_3Cl_4(OAc)_3(py)_3$,[48,52] and $(pyH)_3[Mn_4O_3Cl_7(OAc)_3]$[45]. For convenience, the Mn model compounds will be designated by their special substituent (X, **Cl_4**, or **Cl_7**). XAS samples were made by carefully grinding 5–10 mg of compound and diluting it with a 10-fold excess of boron nitride. The mixture was packed into 0.5-mm-thick Al sample holders and sealed with Mylar windows.

PS II-enriched membranes were isolated from market spinach using a slightly modified BBY preparation,[54,55] with final activities of ~600 ($\mu$mol of $O_2$/mg of Chl)/h. The membranes were resuspended in buffer A (50 mM MES, pH 6, 400 mM sucrose, 5 mM $CaCl_2$) and pelleted by centrifugation at 4 °C and 39000$g$ for 1 h. The pellets were then loaded directly into Lucite sample holders designed to fit into both EPR and X-ray cryostats. The final Mn concentration in these samples was 600–750 $\mu$M Mn, assuming 30 mg of Chl/ mL and 200 Chl/PS II. Samples were dark-adapted in the $S_1$ state, then frozen, stored, and transported in liquid nitrogen. Care was taken to prevent warming of biological samples when they were transferred to the liquid helium cryostat used for EPR and X-ray spectroscopy. The biological samples were characterized with oxygen evolution activity assays and EPR measurements, as described previously.[11]

## X-ray Absorption Spectroscopy

Mn XAS experimental conditions have been previously detailed[11] and are summarized here. XANES and EXAFS spectra were recorded at the wiggler Beamline 7-3 of the Stanford Synchrotron Radiation Laboratory, with a beam current of 65–100 mA at 3.0 GeV. The X-ray beam was used unfocused, with an energy-scanning Si[220] double-crystal monochromator detuned to 50% to attenuate higher harmonics. The compound $Mn_4O_3Br(OAc)_3(dbm)_3$ was measured using a harmonic rejection mirror in the beam path,[56] and ionization chamber detectors ($I_0$, $I_1$, and $I_2$) were filled with dinitrogen. For model compounds, data were collected as fluorescence excitation spectra with a Lytle detector,[57,58] but PS II samples required a 13-element Ge detector.[59] In either case, absorption was related to the fluorescence signal divided by the incident flux ($A = F/I_0$). A liquid-helium flow cryostat (CF1208A, Oxford Instruments) kept the samples at 10 ± 1 K in a gaseous helium atmosphere at ambient pressure. Scans were collected from 6520 to 7100 eV, with step sizes of 0.2 eV in the XANES region (6535–6575 eV), and 0.05 Å$^{-1}$ in the EXAFS region ($k$ = 2–12 Å$^{-1}$). Energy calibration and resolution were monitored by simultaneous measurements of the absorption spectrum of $KMnO_4$, using its narrow preedge line at 6543.3 eV (fwhm ≤1.7 eV). Reproducibility of the Mn K-edge position in the above conditions is typically ±0.1 eV.[18] Four scans were averaged for each Mn compound, whereas PS II required 4 XANES scans and ~20 EXAFS scans.

## Data Analysis

Data reduction for Mn XANES and EXAFS has been detailed earlier and is summarized here.[10,11,18] The preedge background was removed from all spectra by subtracting a linear fit to the preedge region. The data were divided by the Mn free-atom absorption and normalized to the unit edge step by extrapolating a quadratic fit from the postedge region (>7000 eV) to the energy of the edge peak. For XANES spectra, the first inflection-point energy of the steeply rising absorption edge was determined from the zero crossing of the second derivative of the spectrum, produced by analytical differentiation of a third-order polynomial fit to the data over an interval of 3.0 eV on each side of a data point. This

inflection-point energy (IPE) was taken as the K-edge energy position. For EXAFS spectra, a smooth background absorption curve (quadratic fit to the postedge region) was removed from the data to leave the net EXAFS. Conversion from energy space into the photoelectron wave vector[60] ($Å^{-1}$) was done as in eq 1, where $m_e$ is the electron mass, $h$ is Planck's constant, $E$ is the X-ray energy, and $E_0$ is the ionization threshold, chosen as 6563 eV and assigned to the edge peak.

The EXAFS data were weighted by $k^3$, and the low-frequency background was subtracted as a two-domain spline. No windowing function was applied to forward Fourier transforms, but a Hanning

$$k = (2\pi/h) \left[ 2m_c \left( E - E_0 \right) \right]^{1/2} \quad (1)$$

window was used for Fourier filtering. Limits in $k$-space and $R$-space for the forward and back Fourier transforms are shown in Table 1S in the Supporting Information. Fourier peaks were isolated individually and together, to help simplify the analysis and to minimize the effects of distortions from windowing.[61] The resulting Fourier-filtered data were subjected to nonlinear least-squares curve fitting to the EXAFS equation[62] (eq 2) using single-scattering amplitude and phase functions

$$\chi(k) = S_0{}^2 \sum_i N_i B_i(k) \frac{f_{\text{eff}}(\pi, k, R_i)}{k R_i{}^2} \exp\left(-2\sigma^2 K^2\right) \times \exp\left(\frac{-2R_i}{\lambda(k)}\right) \sin\left[2kR_i + 2\delta_i{}^c(k) + \phi_i(k)\right] \quad (2)$$

calculated from the program FEFF 5.05.[63,64] The EXAFS amplitude, $\chi(k)$, is described by eq 2, where, for each shell $i$, $N_i$ is the number of scatterers at a distance $R_i$, $S_0{}^2$ is the many-body amplitude reduction factor, $B_i(k)$ is an amplitude reduction factor caused by inelastic forces in the central atom, $f_{\text{eff}}$ is the effective back-scattering amplitude of the scattering atom, $\delta_i{}^c$ and $\varphi_i$ are the phase shifts for the absorber and back-scatterer, respectively, $\sigma^2$ is the Debye–Waller term, and $\lambda(k)$ is the mean free path of the photoelectron. The basic structure used for calculation of FEFF 5.05 fitting functions ($f_{\text{eff}}$, $\delta$, $\varphi$, $\lambda$) was that of the model complex **OMe**,[47] but other Mn-scatterer interactions were constructed, such as for Mn–F/Cl/Br at distances from 2.2 to 2.8 Å. Curve fitting of the filtered data normally extracts the parameters $R$, $N$, $\sigma^2$, and $\Delta E_0$, where, for each shell, $N$ is the number of scatterers at distance $R$, $\sigma^2$ is the Debye–Waller term, and $\Delta E_0$ is the difference between the ionization threshold $E_0$ of the reference and of the unknown.

Error analysis of the EXAFS fitting results has been discussed elsewhere.[10,30,65,66] The normalized error sum ($\Phi$, eq 3) represents the general quality of the fit, where $N$ is the number of data points and $\chi^{\text{exptl}}(k_i)$ and $\chi^{\text{calcd}}(k_i)$ are the experimental and calculated EXAFS.[65] The normalization factor $s_i$ is defined in eq 4.

$$\Phi = \sum_i^N (1/s_i)^2 \left[ \chi^{\text{exptl}}(k_i) - \chi^{\text{calcd}}(k_i) \right]^2 \quad (3)$$

$$1/s_i = k_i{}^3 / \sum_j^N k_j{}^3 |\chi_j{}^{\text{exptl}}(k_j) \quad (4)$$

Another important indicator of fit quality is a $\chi^2$-like statistic, the $\varepsilon^2$ error (eq 5), which accounts for the number of variable fit parameters ($p$)

$$\epsilon^2 = \left[ N_{\text{ind}} / \left( N_{\text{ind}} - p \right) \right] N^{-1} \Phi \quad (5)$$

and the number of independent data points ($N_{\text{ind}}$). Because the $\varepsilon^2$ error is weighted by the degrees of freedom ($N_{\text{ind}} - p$), the inclusion of additional, unjustified shells of scatterers incurs a penalty, and we can determine whether including more parameters ($p$) actually improves the fit.

Both values are presented here, but curve fitting was done by minimizing the $\Phi$ error specifically, while varying $R$ and $\sigma^2$ for each shell of scatterers. The limited information content in the EXAFS spectrum precludes allowing all four parameters (per shell) $R$, $N$, $\sigma^2$, and $\Delta E_0$ to vary. Especially in the fits to peaks I, II, and III, floating all such variables would result in an underdetermined fit ($p > N_{\text{ind}}$). Therefore, for these whole-spectrum fits, we used only a single $\Delta E_0$ for all shells[10,62] and restricted $N$ to known values from crystallography or previous results.[11] Later, in subsequent two-shell fits to peak II (isolates), $N$ was allowed to float and the observed $N$ was compared to the known values. Coordination numbers are calculated on a per Mn basis and interpreted here in the context of a total of four Mn atoms per PS II. This means that Mn-scatterer interactions appear in multiples of 0.25, except for Mn–Mn interactions, where the increments are 0.5, because each Mn would detect the other at the same distance. Throughout the analysis, data from PS II and the inorganic complexes were processed as uniformly and consistently as possible, especially in the normalization stage, to validate comparisons between the two sets.

## Results

For comparison purposes, the cubanes are subdivided into three groups: the oxygen ("O") cubanes consisting of **OAc**, **OBz**, **OMe**, and **OH**, the "halide" cubanes (**Cl** and **Br**), and the "multiple-halide" cubanes (**Cl$_4$** and **Cl$_7$**). Although **N$_3$** is considered a pseudo-halide, both it and **F** are almost indistinguishable from O by having adjacent atomic numbers, and so **N$_3$** and **F** are grouped with the O cubanes.

### Mn XANES

The Mn K-edge X-ray absorption spectra of the OEC poised in the S$_1$ state and the tetranuclear models **OBz**, **OAc**, **OMe**, **OH**, **N$_3$**, **F**, **Cl**, **Br**, **Cl$_4$**, and **Cl$_7$** are presented in Figure 3 with their corresponding second derivatives presented in Figure 4. Figure 3A shows that the O cubanes resemble the general edge shape of PS II, but differ in the preedge region (6540–6544 eV) and the steeper rise of the K-edge (6549–6553 eV). The inflection-point energy indicates the Mn K-edge position and is defined as the zero crossing of the second derivative (Figure 4). Mn K-edge positions of these compounds are given in Table 1, where the estimated error is ± 0.2 eV, from previous XANES studies.[18] This set of tetranuclear model compounds contains three Mn$^{\text{III}}$ atoms and 1 Mn$^{\text{IV}}$ atom, which is one possible assignment for S$_0$. For **OBz**, **OAc**, **OMe**, **N$_3$**, **F**, and **OH** we find edge positions between 6550.9 and 6551.8 eV (Table 1). These numbers are higher than those reported for the S$_0$ state of PS II, but the second-derivative spectra (see Figure 4) show that the overall edge shape is similar to the one we find for the S$_0$ state in PS II.[18] The spectra of **OBz**, **OAc**, **OMe**, **N$_3$**, **F**, and **OH** (Figure 4A) and PS II in the S$_0$ state[18] lack a feature around 6552 eV, which is present in S$_1$. A positive feature around 6548 eV is also present, with a large amplitude and a significantly narrower width than in S$_1$. The presence of this narrow feature suggests a greater amount of Mn$^{\text{III}}$,[18] and its increased intensity is related to the steeper rising edge in these complexes (Figures 3 and 4). Figure 3B,C shows that the addition of Cl or Br ligands alters the edge shape significantly by shifting to lower energy as seen in the halide cubane compounds **Cl**, **Br**, **Cl$_4$**, and **Cl$_7$** (see also Table 1 and Figure 4B,C). The

exchange of an O atom with one or more Cl atoms (or Br) reduces the ligand hardness and consequently leads to a lower edge position. This is in contrast with **F** and the pseudo-halide **N₃**, which display edge positions within the range of **OBz**, **OAc**, **OMe**, and **OH** (Figure 4A).

We also investigated whether differences in the bond valence sum (BVS) can explain the 1 eV spread that we observe for **OBz**, **OAc**, **OMe**, and **OH**. The bond valence sum analysis (BVSA)[67–69] approach was introduced primarily to assign an oxidation state to a particular metal center on the basis of the knowledge of the nature of the immediate neighbors and the interatomic distances involved. For **OBz**, **OAc**, **OMe**, and **OH** we performed a BVSA using the $r_0$ values reported by Liu and Thorp[70] and the crystallographic Mn–O distances. Within this set of model compounds, there is no change in oxidation states, and all compounds exhibit the same structural motif. An overall average shortening of Mn–O distances is reflected in a higher BVS that correlates with a higher edge position. The BVS values for **OBz**, **OAc**, **OMe**, and **OH** are summarized in Table 1. The four compounds exhibit almost the same number, showing that the BVS concept cannot satisfactorily explain the different edge positions observed here.

## Mn EXAFS

Background-subtracted EXAFS oscillations in *k*-space are presented in Figure 5 for the "oxygen" and "halide" model compounds and PS II. For clarity, the spectra presented in Figure 5 are Fourier-filtered data covering peaks I, II, and III, using the *k*-windows in Table 1S. $k^3$-weighting is applied to offset the decay of EXAFS amplitude at higher *k*-values and to emphasize the contributions of heavier atoms at longer distances. The data sets of the oxygen cubanes **OBz**, **OAc**, **OMe**, **OH**, **N₃**, and **F** are quite similar and almost overlay each other. Although the pattern of oscillations is similar to that of PS II (Figure 5A), the overall amplitude is considerably and consistently larger, and the EXAFS is phase-shifted (at $k = 8$–11.5 Å$^{-1}$). Together these indicate that, although the distances may be similar, the number of such interactions is different from that in PS II. This distinction is most evident in the Fourier transforms that are shown in Figure 6 and discussed below. The halide cubanes are unique for their incorporation of a single halide into a tetranuclear Mn cluster.[45,50] Of these, the single halides **F**, **Cl**, and **Br** are again similar to each other (Figure 5B), but distinct from PS II, in amplitude and phase. When more chloride atoms are ligated to Mn in **Cl₄** and **Cl₇** (Figure 5C), the EXAFS oscillation pattern changes drastically, but it should be noted that these two compounds have aromatic pyridine ligands.

Mn EXAFS spectra were truncated to $k = 11.7$ Å$^{-1}$ starting from $k = 3.3$ Å$^{-1}$ (see Table 1S; forward Fourier transform parameter). The Fourier transforms of the raw *k*-space data of **OBz**, **OAc**, **OMe**, **OH**, **N₃**, **F**, and PS II are presented in Figure 6A, while those of **Cl** and **Br** and PS II appear in Figure 6B. The multiple-halide cubanes **Cl₄** and **Cl₇** are shown in Figure 6C. Two and sometimes three peaks appear at $R' = 1.4$–1.5 Å (I), 2.3–2.5 Å (II), and 2.9–3.0 Å (III), which are clearly above the noise level. All peaks appear at an apparent distance $R'$ that is shorter than the actual distances by 0.4–0.5 Å due to a phase shift. The shoulder below $R' = 1$ Å is a result of incomplete background removal. Compared to PS II, the larger magnitude of the Fourier transforms imply a larger number of ordered contributions to peaks I and II (and III for OBz), and the longer peak distances imply longer averaged distances for those interactions. The most obvious difference between PS II and the cubane model compounds is in the intensities of peaks I and II (Figure 6A,B); those of PS II are much lower. For all other compounds, with the exception of **OBz**, "peak III" appears as a shoulder on peak II. Whereas PS II shows a resolved peak III, only the **OBz** cubane shows a comparable feature, at a slightly longer distance. Another difference is the significant scattering contribution between peaks I and II shown by **Cl₄** and **Cl₇** (Figure 6C),

as manifested by a shoulder at $R' = 1.9$–$2.0$ Å or a broadening of peak II. These compounds exhibit three and six terminal Cl ligands, respectively, at 2.25 Å besides one bridging Cl at 2.65 Å.

Peaks I and II (and III) have been isolated by Fourier filtering (Figure 5) for curve-fitting analysis. They have been isolated and analyzed both individually and collectively, but only the results from group fitting will be described here. The curve-fit range was $k = 3.3$–$11.7$ Å$^{-1}$. To keep the number of variable parameters from exceeding the number of independent data points and prevent underdetermined fits, the coordination numbers ($N$, per four Mn atoms) for the cubanes were fixed to crystallographically known values. For PS II, we used $N$ values determined previously.[11] Also, one $\Delta E_0$ value was used for all shells in each fit, following previous practice.[10,62] For the oxygen cubanes (including **F** and **N₃**), three to four shells were used except for **OBz**, which required five shells. For the halides (**Cl**, **Br**, **Cl₄**, **Cl₇**) four to five shells were used, and we found that a sixth shell did not significantly improve the fit. To evaluate the fits, we monitored the $\varepsilon^2$ error to see whether the addition of more shells (and more variables) actually improved the fit.

We compared the best fit distances to the crystallographically determined values, which were segregated by shells consisting of a number of neighbors centered at an average distance. The theoretical model used by the FEFF 5.05 program was the **OMe** cubane, from which we generated Mn-scatterer phase and amplitude functions as needed for curve fitting. Only single-scattering functions were used, and we tried to fit only the Mn nearest neighbors and the Mn cubane core. The fit results are tabulated in Table 2, where almost all distances were fit to within ±0.05 Å of the crystallographic values.

For **OBz**, **OAc**, **OMe**, and **OH**, two nearest-neighbor oxygen shells were resolved, with 4.5 O atoms at ~1.9 Å and another 1.5 O atoms at ~ 2.2 Å. This difference is greater than the EXAFS resolution limit ($\Delta R = \pi/2\Delta k = 0.196$ Å).[35,71] The best fit spectra for **OH**, **OMe**, **OAc**, and **OBz** are shown in Figure 7. Except for **OBz**, these O cubanes were reasonably fit with four distinct shells: two each of oxygen, and two of Mn. N and F are normally indistinguishable from O by EXAFS, the $\mu_3$-X atom was combined into the longer Mn–O interaction (~2.2 Å). The best fit spectra for **N₃** and **F** appear in Figure 8. For the most highly distorted cubane **OBz**, five shells were needed to describe the core: two shells of O (1.9 and 2.2 Å) and three shells of Mn (2.8, 3.2, and 3.4 Å). Again, the differences in distances are above the resolution limit, allowing us to distinguish the three Mn shells. The fit error is reduced by 40% when the fifth shell is included. The heterogeneity in the longer Mn–Mn distance allows peak III to be separated from peak II. In general, peak II (and III for **OBz**) consists of two sets of Mn–Mn distances: a short one ($N = 1.5$) at 2.79–2.83 Å and a longer one ($N = 1.5$) at 3.12–3.37 Å. The model compounds with smaller differences between these two vectors, such as **OMe** (0.31 Å), **OAc** (0.35 Å), **OH** (0.28 Å), **N₃** (0.35 Å), **Br** (0.39 Å), and **F** (0.30 Å), show only a shoulder on the right side of peak II (Figure 5). However, for the cubanes with larger differences, such as **Cl** (0.45 Å), **Cl₄** (0.46 Å), and **Cl₇** (0.45 Å), peak II begins to be resolved. The cubane with the largest difference between the Mn–Mn vectors, **OBz** (0.56 Å), has the most clearly resolved peak III (Figure 6A).

For the halide cubanes **Cl**, **Br**, **Cl₄**, and **Cl₇**, there are distinct halide shells, which were detected by EXAFS: terminal Cl at 2.2–2.3 Å, and bridging Cl$^-$ (or Br$^-$) at 2.6–2.7 Å (Table 2 and Figure 9). Except for the Mn–Br vector, these distances were determined to within ±0.05 Å of the known values (Table 2). We found that, for **Cl₄** and **Cl₇**, five shells could adequately describe the EXAFS spectra; the sixth shell of longer Mn–O (2.2 Å) either did not improve the $\varepsilon^2$ error or gave unrealistic distances. For comparison, the fit to the filtered data for PS II, using results derived previously,[11] is shown in Figure 8. In this simplistic three-shell fit, the distances for the O shell (1.85 Å) and the 2.7 Å Mn–Mn shell are shorter

than those found in the Mn cubanes. The derived coordination numbers for PS II are smaller than their counterparts in the Mn cubanes, accounting partly for the reduced amplitude in the EXAFS and FT.

To assess the accuracy of the method in determining coordination numbers for the crucial metal–metal vectors, we isolated the Fourier peak II (with peak III, when applicable) and simulated with short (~2.8 Å) and long (~3.2 Å) Mn–Mn distances. In the previous whole-spectrum fits (Table 2), the coordination numbers were fixed to known values to avoid underdetermined fits and reduce complexity. For the isolated peak II fits, though, *N* is allowed to vary and the cubanes are treated as "unknown" structures in a manner similar to that for PS II. These unrestrained fits allow us to compare directly the *N* from the PS II and the cubanes, and gauge the uncertainty associated with this parameter for the crucial Mn–Mn vectors. The fitting results are presented in Table 3. Except for **OBz**, only two shells (long and short Mn–Mn) are used to reduce the complexity and avoid underdetermined fits resulting from too many floating parameters. Also, only the six O cubanes were simulated to avoid interference and complications (more shells) introduced by the Mn–halide vector in the Mn halide cubanes (**Cl**, **Br**, **Cl4**, and **Cl7**). These O cubanes are compared directly with a similar unrestrained *N* fit for PS II in Table 3, and similar trends can be expected for the halide cubanes.

Table 3 shows that the unrestrained *N* for the Mn–Mn 2.8 Å vector differs from the known values by an average of 13%, up to a maximum deviation of about 30%. Likewise, the *N* for the longer Mn–Mn (~3.2 Å) vector deviates from the true *N* by an average of 18%, also with a maximum error of 30%. These uncertainties for the coordination numbers agree with the previously discussed limitation of the EXAFS technique.[11,35] In comparing these unconstrained *N* fits of the Mn O cubanes with PS II, we find the *N* for the Mn–Mn 2.8 Å vector is almost always larger than that from PS II, while the $N_{3.2 \text{ Å}}$ is always greater than that from the corresponding PS II vector. Even allowing for the maximum possible error in *N*, the discrepancy in the coordination numbers for the Mn–Mn distances between the Mn cubanes and PS II remains significant and sizable. Accordingly, the ratio between the long and short Mn–Mn vectors for PS II is twice that of the cubanes.

## Discussion

### Mn XANES Spectra

The O cubanes (**OH**, **OMe**, **OAc**, and **OBz**) along with **F** and **N3** exhibit Mn K-edge spectra superficially similar to that of PS II ($S_1$ state, Figure 3A), and the edge positions fall between those of the $S_0$ and $S_1$ states (Table 1). The qualitative similarity may be due in part to the absence of $Mn^{II}$ and the nearly exclusive O ligation environment. This O ligation is a property that these cubanes share with PS II, although PS II has a histidine ligand.[72] The presence of aromatic N ligands (such as pyridine) adds more structure to the edge, altering the edge shape considerably to make it distinct from that of PS II (R. Cinco, unpublished results). The qualitative similarity in the XANES is not present in the second-derivative spectra (Figure 4), which are all distinct from that of PS II and indicate strongly the presence of $Mn^{III}$.[18] This is not surprising, because the oxidation state distributions are different: PS II ($S_1$) has two $Mn^{III}$ atoms and two $Mn^{IV}$ atoms, whereas the cubanes have three $Mn^{III}$ atoms and one $Mn^{IV}$ atom present. The XANES from the halide cubanes look different from that from PS II, especially in the edge shift to lower energy (Table 2, Figures 3B,C and 4B,C). The lower energy is indicative of halide ligation, because the presence of the electronegative halide reduces the X-ray energy required to ionize the K-shell (1s) electron. The presence of bridging Cl in the **Cl** cubane lowers the edge energy more than does the addition of terminal Cl ligands in **Cl4** and **Cl7** (Figures 3C and 4C, Table 1), probably

because the bridging Cl provides more covalency in the Mn–Cl bond than does the terminal Cl.[73]

## Mn EXAFS and FT

Superficial similarities in the FTs between the cubanes and PS II mostly fade in light of the EXAFS and in subsequent curve fitting. Upon comparing the $k^3$-weighted EXAFS from **OBz**, **OAc**, **OMe**, **OH**, **N₃**, and **F** among themselves and to that from PS II (Figure 5A), the differences are immediately apparent. Although the Mn cubanes simulate the oscillation pattern of PS II, because they contain both ~ 2.8 and ~ 3.2 Å vectors, the normalized amplitudes are larger and are phase-shifted at $k = 8–11$ Å$^{-1}$. The EXAFS from the O cubanes (Figure 5A, except **OBz**) are very similar to one another and to those from **F** and **N₃**, while only the most distorted one (**OBz**) stands out, especially at $k = 8.5$ Å$^{-1}$. Among the halides, **Br** is distinguishable from **Cl** by the pattern at $k = 8–9$ Å$^{-1}$ (Figure 5B), while the **Cl₄** and **Cl₇** have oscillation patterns distinct from those of the rest of the Mn cubanes and from that of PS II (Figure 5C). Thus, from the EXAFS spectra, the three categories of cubanes now divide into four: (1) **OMe**, **OH**, **OAc**, **N₃**, and **F**; (2) **OBz**; (3) **Cl** and **Br**; and (4) **Cl₄** and **Cl₇**. None of these categories reproduces the observed PS II EXAFS spectrum (S₁) in amplitude or phase.

In the analysis of the Mn EXAFS, we obtained reasonably good fits by using single-scattering, theoretical FEFF-generated phases and amplitudes, and focusing only on the core structure of the cubane. Once the coordination numbers were fixed to known values, we obtained highly accurate distances, to within ±0.05 Å of the known values (except for **Br**). By using only four to five shells of scatterers, we could accurately describe the EXAFS spectra of the cubanes (Figures 7–9). In particular we could resolve the three Mn–Mn vectors in **OBz**, where two such vectors are 0.56 Å apart, leading to a resolved peak III. EXAFS could also detect the Mn–Cl (Br) bridging interaction in **Cl₄**, **Cl₇**, **Cl**, and **Br**, and the terminal Cl ligands in **Cl₄** and **Cl₇** at 2.22 Å (three Cl atoms) and 2.27 Å (six Cl atoms), respectively.

In the Fourier transforms (Figure 6), only **OBz** shows a clearly resolved peak III comparable to that of PS II, but at longer distance. In the other model compounds, peak III appears mostly as a shoulder of peak II. The most obvious difference between the cubanes and PS II is the larger magnitude of peaks I and II; only **Cl₄** approaches PS II in FT magnitude (Figure 6C), but its EXAFS is very different. Also, even though **OBz** has three peaks like PS II, its EXAFS amplitude and FT magnitude exceed that of PS II. In addition, the FTs for **Cl₄** and **Cl₇** (Figure 6C) reveal the presence of a significant scattering contribution between peaks I and II (a shoulder at $R' = 1.9–2.0$ Å) arising from three or six terminal Cl ligands, respectively. For the distorted cubanes, peak I appears at a longer distance in the FT than the corresponding peak in PS II and indicates there must be more $\mu_2$-oxo bridging in PS II. The $\mu_3$-O bridges in the cubanes give relatively longer Mn–O distances. Peak I is also larger because of the greater number of Mn–O (short) distances in the cubanes (4.5 vs 2.5, Table 2). The nonbridging Mn–O distances in the PS II may also be more disordered compared to those in the cubanes so that only the shorter $\mu$-oxo bridges are detected, while in the cubane EXAFS, both the long and short Mn–O bonds contribute.

The ratio of first to second Fourier peaks (Figure 6) cannot be used to assign either the arrangement of the Mn atoms or the number of Mn–Mn distances. The intensity of the first peak depends on the number and distribution of bridging and terminal ligand distances. Unlike the case of Fe–S clusters, where the ratio of first-to-second peaks suggests the ratio of Fe–S to Fe–Fe vectors,[74] such a first-to-second peak ratio does not necessarily predict the number of Mn–O to Mn–Mn vectors for either PS II or the cubanes. The number of Fe–S vs

Fe–Fe vectors correlates with the first-to-second peak ratios because of the very similar distances of bridging and terminal Fe-S bonds (within 0.1 Å).[75,76] In the case of the Mn clusters, however, the bridging and terminal Mn–O distances are distributed over a wider range (0.3 Å; see Table 2). This distribution of distances, summarized in the Debye–Waller factor in the EXAFS equation (eq 2), leads to destructive interference from these O ligands that attenuates and broadens the first Fourier peak. Hence, such relative similarity in Fourier peak ratios here is incidental and does not imply that PS II and the cubanes share similar numbers of Mn–O and Mn–Mn vectors. Only through curve fitting of the $k$-space EXAFS (and not Fourier peak heights alone) can these Mn–O vs Mn–Mn ratios and numbers be derived quantitatively (Tables 2 and 3).

There is also a large difference in peak II intensity compared to that in PS II (Figure 6). In the cubanes, there is a short Mn–Mn vector ($N_{short}$ = 1.5) at 2.8 Å and a longer Mn–Mn ($N_{long}$ = 1.5) at 3.2–3.3 Å. This pattern is different from the dimer-of-dimers model, which gives a 2.7 Å Mn–Mn vector ($N_{short}$ = 1.0) and a longer one at 3.3 Å ($N_{long}$ = 0.5). The disparity in the amplitudes of the Fourier transforms in Figure 6 cannot simply be explained by invoking more disorder in the native OEC. Rather, the Fourier peak II amplitude is larger because $N_{2.8 Å}$ is greater (1.5 > 1.0) and there is contribution from the nearby longer Mn–Mn distance: $N_{3.2 Å}$ = 1.5. Although the distances of Mn–Mn vectors are similar, the distribution of $N$ dictates the arrangement of short and long Mn–Mn distances and serves to differentiate the possible models for PS II as depicted in Figure 1. By comparing such $N$ patterns, we can exclude the distorted cubane with $C_{3v}$ symmetry as a structural analogue to the native Mn cluster. This is consistent with the $S$ = 9/2 ground states of these species, which already showed structural noncongruence with the OEC.[45–47]

To focus on the crucial Mn–Mn vectors, we isolated Fourier peak II from the rest of the EXAFS and simulated it with long and short distances. By not constraining $N$ to crystallographic values, we tested the accuracy of determining coordination numbers through EXAFS. A more balanced comparison between the cubanes and PS II was then made by treating both as "unknown" structures (regarding the Mn–Mn vectors). As Table 3 shows, even when $N$ is allowed to float freely during the fits, the observed coordination numbers do not deviate much from the true values. Observed errors range from averages of 13% ($N_{short}$) and 18% ($N_{long}$) up to a maximum of 30%. These are within the limitations of the EXAFS technique as determined previously.[11,35] Despite these errors in $N$, the disparities in Mn–Mn vectors between the Mn cubanes and PS II remain significant. Except for **OBz**, in the O cubanes, the ratio of $N_{short}$ to $N_{long}$ approaches 1, whereas the PS II ratio is closer to 2. In addition, the absolute values of $N$ are almost always larger in the cubanes. This shows that the $C_{3v}$ distorted cubanes are still too symmetric to resemble the OEC active site.

Even though this study has shown that the $C_{3v}$ Mn cubanes cannot be a structural analogue for the OEC, the cubanes do point to future synthetic approaches for modeling the OEC active site. Clearly, more distortion in the cubane framework is needed, as shown by the **OBz** cubane, whose EXAFS and FT come closest (out of the 10) to resembling those of PS II. Future synthetic biomimetic efforts should focus on adding even more distortion, to alter the ratio of long to short Mn–Mn distances. Also, the nearly exclusive oxygen ligation (except for **Cl4** and **Cl7**) present in these cubanes is a positive advance that should continue to be incorporated in subsequent models.

## Conclusion

We have shown through a combination of $k$-space Mn EXAFS, Fourier transform, and curve-fitting analyses that the distorted-cubane model of $C_{3v}$ symmetry is excluded as a

topological model for the Mn cluster in the OEC. Of the 10 cubane complexes studied, only the most distorted (**OBz**) comes closest to resembling PS II, emphasizing the need for even more distortion of the cubane framework to approach the observed OEC data. Among the remaining topological possibilities, the dimer-of-dimers model continues to be favored, for reasons discussed previously.[11] We have shown the ability of EXAFS to verify the known core structure of these cubanes, by starting from theoretical phases and amplitudes and using only the simple core structure to simulate the experimental spectra. Mn EXAFS also is able to detect small changes in the cubane structure in going from the oxygen cubanes (**OAc**, **OMe**, **OH**, **F**, **N$_3$**) to the halide cubanes (**Cl**, **Br**), to the multiple-halide cubanes (**Cl$_4$**, **Cl$_7$**), and finally to the most distorted **OBz**. Just as EXAFS has been employed to determine the degree of discrepancy between the $C_{3v}$ symmetry distorted cubane and the OEC, this tool can be used to test other synthetic bioinorganic complexes for their resemblance and relevance to the Mn cluster in PS II.

## Supplementary Material

Refer to Web version on PubMed Central for supplementary material.

## Acknowledgments

## References

1. Debus RJ. Biochim. Biophys. Acta. 1992; 1102:269–352. [PubMed: 1390827]

2. Rutherford, AW.; Zimmermann, J-L.; Boussac, A. The Photo-systems: Structure, Function, and Molecular Biology. Barber, J., editor. Elsevier B. V.; Amsterdam: 1992. p. 179-229.

3. Renger, G. Bioenergetics. Gräber, P.; Milazzo, G., editors. Birkhäuser Verlag; Basel, Switzerland: 1997. p. 310-358.

4. Yachandra VK, Sauer K, Klein MP. Chem. ReV. 1996; 96:2927–2950. [PubMed: 11848846]

5. Kok B, Forbush B, McGloin M. Photochem. Photobiol. 1970; 11:457–476. [PubMed: 5456273]

6. Britt, RD. Oxygenic Photosynthesis: The Light Reactions. Ort, DR.; Yocum, CF., editors. Kluwer Academic Publishers; Dordrecht: 1996. p. 137-164.

7. Wieghardt K. Angew. Chem., Int. Ed. Engl. 1994; 33:725–728.

8. Yachandra VK. Methods Enzymol. 1995; 246:638–675. [PubMed: 7752941]

9. Yachandra VK, DeRose VJ, Latimer MJ, Mukerji I, Sauer K, Klein MP. Science. 1993; 260:675–679. [PubMed: 8480177]

10. Latimer MJ, DeRose VJ, Mukerji I, Yachandra VK, Sauer K, Klein MP. Biochemistry. 1995; 34:10898–10909. [PubMed: 7662671]

11. DeRose VJ, Mukerji I, Latimer MJ, Yachandra VK, Sauer K, Klein MP. J. Am. Chem. Soc. 1994; 116:5239–5249.

12. George GN, Prince RC, Cramer SP. Science. 1989; 243:789–791. [PubMed: 2916124]

13. Riggs-Gelasco PJ, Mei R, Ghanotakis DF, Yocum CF, Penner-Hahn JE. J. Am. Chem. Soc. 1996; 118:2400–2410.

14. Riggs-Gelasco PJ, Mei R, Yocum CF, Penner-Hahn JE. J. Am. Chem. Soc. 1996; 118:2387–2399.

15. Penner-Hahn JE, Fronko RM, Pecoraro VL, Yocum CF, Betts SD, Bowlby NR. J. Am. Chem. Soc. 1990; 112:2549–2557.

16. MacLachlan DJ, Hallahan BJ, Ruffle SV, Nugent JHA, Evans MCW, Strange RW, Hasnain SS. Biochem. J. 1992; 285:569–576. [PubMed: 1637347]

17. Cinco RM, Robblee JH, Rompel A, Fernandez C, Yachandra VK, Sauer K, Klein MP. J. Phys. Chem. B. 1998; 102:8248–8256.

18. Roelofs TA, Liang W, Latimer MJ, Cinco RM, Rompel A, Andrews JC, Sauer K, Yachandra VK, Klein MP. Proc. Natl. Acad. Sci. U.S.A. 1996; 93:3335–3340. [PubMed: 11607649]

19. Ono T-A, Noguchi T, Inoue Y, Kusunoki M, Matsushita T, Oyanagi H. Science. 1992; 258:1335–1337. [PubMed: 17778358]

20. Ono T-A, Kusunoki M, Matsushita T, Oyanagi H, Inoue Y. Biochemistry. 1991; 30:6836–6841. [PubMed: 1648962]

21. Iuzzolino L, Dittmer J, Dörner W, Meyer-Klaucke W, Dau H. Biochemistry. 1998; 37:17112–17119. [PubMed: 9860823]

22. Roelofs, TA.; Liang, W.; Latimer, MJ.; Cinco, RM.; Rompel, A.; Andrews, JC.; Yachandra, VK.; Sauer, K.; Klein, MP. Photosynthesis: From Light to Biosphere. Mathis, P., editor. Vol. II. Kluwer; Dordrecht, The Netherlands: 1995. p. 459-462.

23. Yocum, CF. Manganese Redox Enzymes. Pecoraro, VL., editor. VCH Publishers; New York: 1992. p. 71-84.

24. Homann PH. Biochim. Biophys. Acta. 1988; 934:1–13.

25. Coleman WJ. Photosynth. Res. 1990; 23:1–27. [PubMed: 24420988]

26. Lindberg K, Andréasson L-E. Biochemistry. 1996; 35:14259–14267. [PubMed: 8916911]

27. McDermott AE, Yachandra VK, Guiles RD, Cole JL, Dexheimer SL, Britt RD, Sauer K, Klein MP. Biochemistry. 1988; 27:4021–4031. [PubMed: 2843222]

28. Yachandra VK, Guiles RD, McDermott AE, Cole JL, Britt RD, Dexheimer SL, Sauer K, Klein MP. Biochemistry. 1987; 26:5974–81. [PubMed: 3318924]

29. Fernandez, C.; Cinco, RM.; Robblee, JH.; Messinger, J.; Pizarro, SA.; Sauer, K.; Yachandra, VK.; Klein, MP. Photosynthesis: Mechanisms and Effects. Garab, G., editor. Kluwer Academic Publishers; Dordrecht, The Netherlands: 1998. p. 1399-1402.

30. DeRose VJ, Latimer MJ, Zimmermann J-L, Mukerji I, Yachandra VK, Sauer K, Klein MP. Chem. Phys. 1995; 194:443–459.

31. Rüttinger W, Dismukes GC. Chem. Rev. 1997; 97:1–24. [PubMed: 11848863]

32. Andréasson, L-E.; Vänngård, T. Encyclopedia of Inorganic Chemistry. King, RB., editor. Vol. 4. John Wiley & Sons; Chichester: 1994. p. 2101-2118.

33. Larson, EJ.; Pecoraro, VL. Manganese Redox Enzymes. Pecoraro, VL., editor. VCH Publishers; New York: 1992. p. 1-28.

34. Pecoraro, VL. Manganese Redox Enzymes. Pecoraro, VL., editor. VCH Publishers; New York: 1992. p. 197-231.

35. Riggs-Gelasco PJ, Stemmler TL, Penner-Hahn JE. Coord. Chem. Rev. 1995; 144:245–286.

36. Stemmler TL, Sossong TM Jr. Goldstein JI, Ash DE, Elgren TE, Kurtz DM Jr. Penner-Hahn JE. Biochemistry. 1997; 36:9847–9858. [PubMed: 9245417]

37. Tommos C, Babcock GT. Acc. Chem. Res. 1998; 31:18–25.

38. Brudvig GW, Crabtree RH. Proc. Natl. Acad. Sci. U.S.A. 1986; 83:4586–4588. [PubMed: 3460059]

39. Vincent JB, Christmas C, Huffman JC, Christou G, Chang H-R, Hendrickson DN. J. Chem. Soc., Chem. Commun. 1987:236–238.

40. Guiles RD, Zimmermann J-L, McDermott AE, Yachandra VK, Cole JL, Dexheimer SL, Britt RD, Wieghardt K, Bossek U, Sauer K, Klein MP. Biochemistry. 1990; 29:471–485. [PubMed: 2154247]

41. Guiles RD, Yachandra VK, McDermott AE, Cole JL, Dexheimer SL, Britt RD, Sauer K, Klein MP. Biochemistry. 1990; 29:486–496. [PubMed: 2154248]

42. George GN, Prince RC, Frey TG, Cramer SP. Physica B. 1989; 158:81–83.

43. Mukerji I, Andrews JC, DeRose VJ, Latimer MJ, Yachandra VK, Sauer K, Klein MP. Biochemistry. 1994; 33:9712–21. [PubMed: 8068650]

44. Yachandra VK, DeRose VJ, Latimer MJ, Mukerji I, Sauer K, Klein MP. Jpn. J. Appl. Phys. 1993; 32:523–526.

45. Wang S, Tsai H-L, Libby E, Folting K, Streib WE, Hendrickson DN, Christou G. Inorg. Chem. 1996; 35:7578–7589.

46. Wemple MW, Adams DM, Folting K, Hendrickson DN, Christou G. J. Am. Chem. Soc. 1995; 117:7275–7276.

47. Aromí G, Wemple MW, Aubin SJ, Folting K, Hendrickson DN, Christou G. J. Am. Chem. Soc. 1998; 120:5850–5851.

48. Wemple MW, Tsai H-L, Folting K, Hendrickson DN, Christou G. Inorg. Chem. 1993; 32:2025–2031.

49. Wemple MW, Adams DM, Hagen KS, Folting K, Hendrickson DN, Christou G. J. Chem. Soc., Chem. Commun. 1995:1591–1593.

50. Wang S, Folting K, Streib WE, Schmitt EA, McCusker JK, Hendrickson DN, Christou G. Angew. Chem., Int. Ed. Engl. 1991; 30:305–306.

51. Wang S, Tsai H-L, Hagen KS, Hendrickson DN, Christou G. J. Am. Chem. Soc. 1994; 116:8376–8377.

52. Hendrickson DN, Christou G, Schmitt EA, Libby E, Bashkin JS, Wang S, Tsai H-L, Vincent JB, Boyd PDW, Huffman JC, Folting K, Li Q, Streib WE. J. Am. Chem. Soc. 1992; 114:2455–2471.

53. Sauer, K.; Yachandra, VK.; Britt, RD.; Klein, MP. Manganese Redox Enzymes. Pecoraro, VL., editor. VCH Publishers; New York: 1992. p. 141-175.

54. Berthold DA, Babcock GT, Yocum CF. FEBS Lett. 1981; 134:231–234.

55. Dunahay TG, Staehelin LA, Seibert M, Ogilvie PD, Berg SP. Biochim. Biophys. Acta. 1984; 764:179–193.

56. Latimer MJ, Rompel A, Underwood JH, Yachandra VK, Klein MP. Rev. Sci. Instrum. 1995; 66:1843–1845.

57. Stern EA, Heald SM. Rev. Sci. Instrum. 1979; 50:1579. [PubMed: 18699438]

58. Lytle FW, Greegor RB, Sandstrom DR, Marques EC, Wong J, Spiro CL, Huffman GP, Huggins PE. Nucl. Instrum. Methods. 1984; 226:542–548.

59. Cramer SP, Tench O, Yocum M, George GN. Nucl. Instrum. Methods Phys. Res. 1988; A266:586–591.

60. Teo, BK. EXAFS: Basic Principles and Data Analysis. Springer-Verlag; Berlin: 1986.

61. Zhang K, Stern EA, Ellis F, Sanders-Loehr J, Shiemke AK. Biochemistry. 1988; 27:7470–7479. [PubMed: 3207685]

62. O'Day PA, Rehr JJ, Zabinsky SI, Brown GE Jr. J. Am. Chem. Soc. 1994; 116:2938–2949.

63. Rehr JJ, Mustre de Leon J, Zabinsky SI, Albers RC. J. Am. Chem. Soc. 1991; 113:5135–5140.

64. Rehr JJ, Albers RC, Zabinsky SI. Phys. Rev. Lett. 1992; 69:3397–3400. [PubMed: 10046808]

65. Binsted N, Strange RW, Hasnain SS. Biochemistry. 1992; 31:12117–12125. [PubMed: 1280998]

66. Bunker, GA.; Hasnain, SS.; Sayers, DE. X-ray Absorption Fine Structure. Hasnain, SS., editor. Ellis Horwood; New York: 1991. p. 751-770.

67. Palenik GJ. Inorg. Chem. 1997; 36:4888–4890. [PubMed: 11670170]

68. Palenik GJ. Inorg. Chem. 1997; 36:3394–3397. [PubMed: 11670011]

69. Palenik GJ. Inorg. Chem. 1997; 36:122.

70. Liu W, Thorp HH. Inorg. Chem. 1993; 32:4102–4105.

71. Clark-Baldwin K, Tierney DL, Govindaswamy N, Gruff ES, Kim C, Berg J, Koch SA, Penner-Hahn JE. J. Am. Chem. Soc. 1998; 120:8401–8409.

72. DeRose VJ, Yachandra VK, McDermott AE, Britt RD, Sauer K, Klein MP. Biochemistry. 1991; 30:1335–134. [PubMed: 1846751]

73. Rompel A, Andrews JC, Cinco RM, Wemple MW, Christou G, Pecoraro VL, Sauer K, Yachandra VK, Klein MP. J. Am. Chem. Soc. 1997; 119:4465–4470.

74. Teo, B-K.; Shulman, RG. Iron-Sulfur Proteins. Spiro, TG., editor. John Wiley & Sons; New York: 1982. p. 343-366.

75. Berg, JM.; Holm, RH. Iron-Sulfur Proteins. Spiro, TG., editor. John Wiley & Sons; New York: 1982. p. 1-66.

76. Stout, CD. Iron-Sulfur Proteins. Spiro, TG., editor. John Wiley & Sons; New York: 1982. p. 97-146.
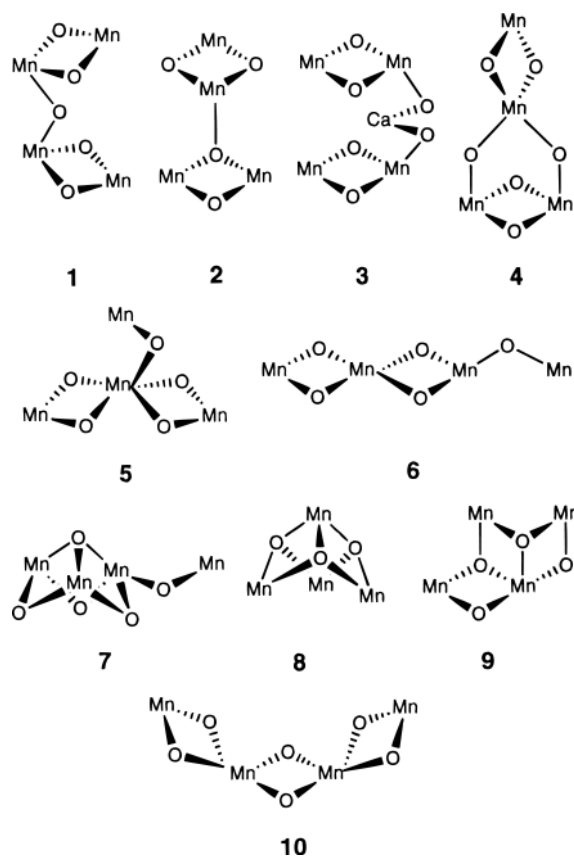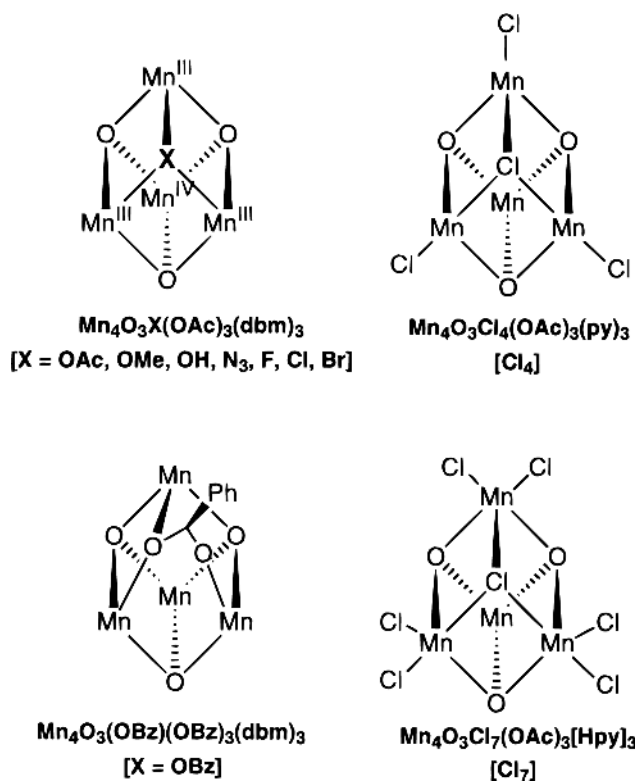
**Figure 1.**
Possible core structures for the active site of the OEC in PS II, containing Mn–Mn distances of 2.7–2.8 and 3.1–3.3 Å. Reprinted from ref 11. Copyright 1994 American Chemical Society. Only Mn and bridging O are shown.

$Mn_4O_3X(OAc)_3(dbm)_3$
[X = OAc, OMe, OH, N$_3$, F, Cl, Br]

$Mn_4O_3Cl_4(OAc)_3(py)_3$
[Cl$_4$]

$Mn_4O_3(OBz)(OBz)_3(dbm)_3$
[X = OBz]

$Mn_4O_3Cl_7(OAc)_3[Hpy]_3$
[Cl$_7$]

**Figure 2.**
Core structures of tetranuclear Mn cubane complexes: $[Mn_4O_3X(OAc)_3(dbm)_3]$ (with X = **OAc**, **OMe**, **OH**, **N$_3$**, **F**, **Cl**, **Br**), $[Mn_4O_3(\textbf{OBz})(OBz)_3(dbm)_3]$, $Mn_4O_3\textbf{Cl}_\textbf{4}(OAc)_3(py)_3$ and $(pyH)_3[Mn_4O_3\textbf{Cl}_\textbf{7}(OAc)_3]$. Carboxylate bridges and other terminal ligands outside the cubane framework are not depicted.
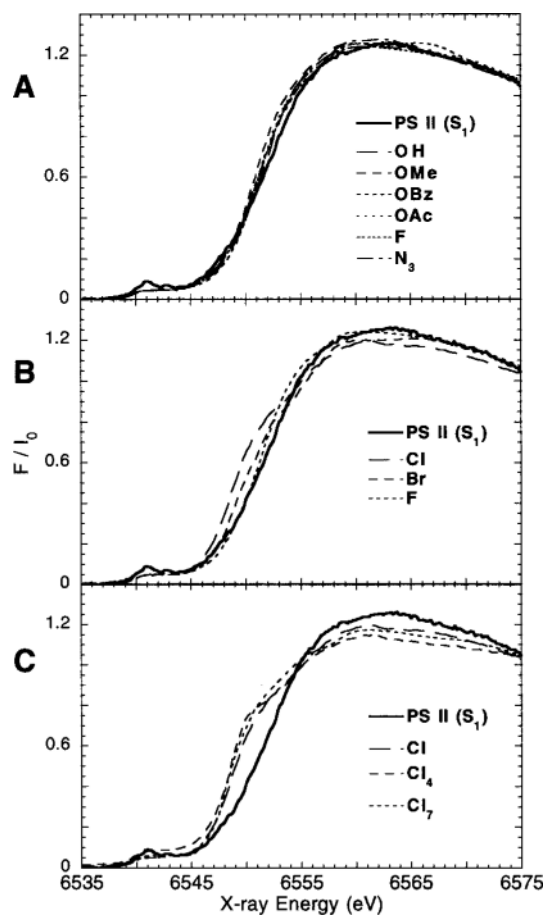
**Figure 3.**
Normalized Mn K-edge X-ray absorption near-edge structure (XANES) spectra of spinach photosystem II (PS II) preparations poised in the $S_1$ state and model compounds: (A) **OBz**, **OAc**, **OMe**, **OH**, **N$_3$**, and **F**; (B) **F**, **Cl**, **Br**; (C) **Cl**, **Cl$_4$**, and **Cl$_7$**.
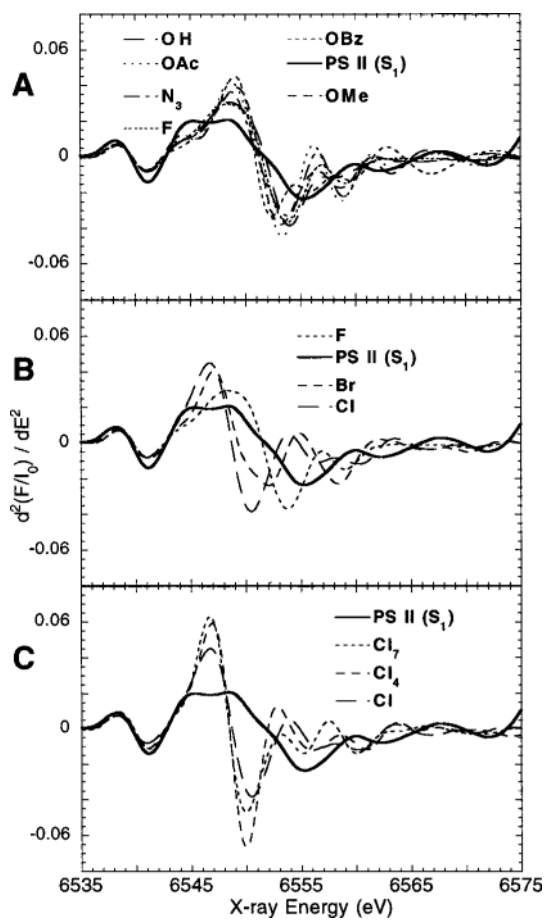
**Figure 4.**
(A) Second derivatives of the edge region of the samples in Figure 2A. (B) Second derivatives of the edge region of the samples in Figure 2B. (C) Second-derivative spectra of XANES from Figure 2C. Data were smoothed by a cubic polynomial fit over ±3.0 eV around each point.
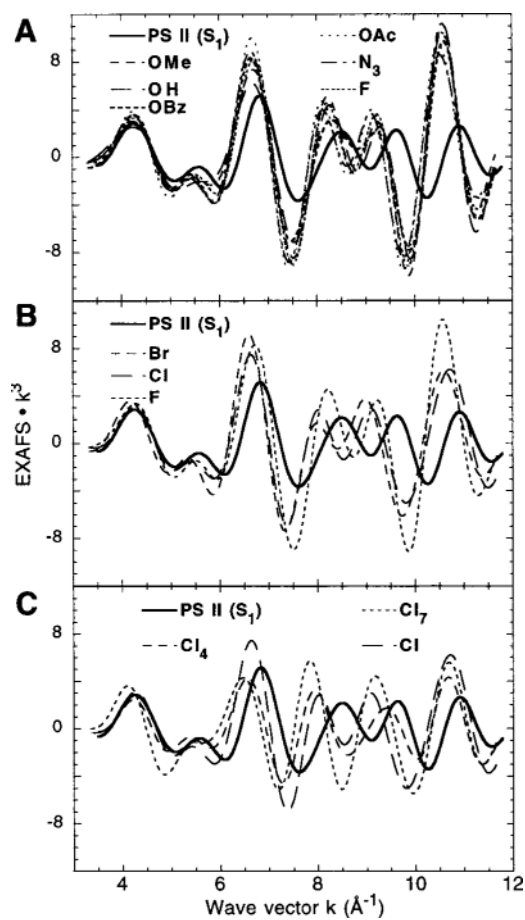
**Figure 5.**
Background-subtracted $k$-space EXAFS from PS II in the $S_1$ state and model compounds. For clarity, the EXAFS are Fourier-filtered using the $\Delta R$ ranges in Table 1S, and have been weighted by $k^3$. The raw $k$-space EXAFS spectra are available in Figure 1S. (A) **OBz**, **OAc**, **OMe**, **OH**, **N₃**, and **F**; (B) **F**, **Cl**, and **Br**; (C) **Cl**, **Cl₄**, and **Cl₇**.
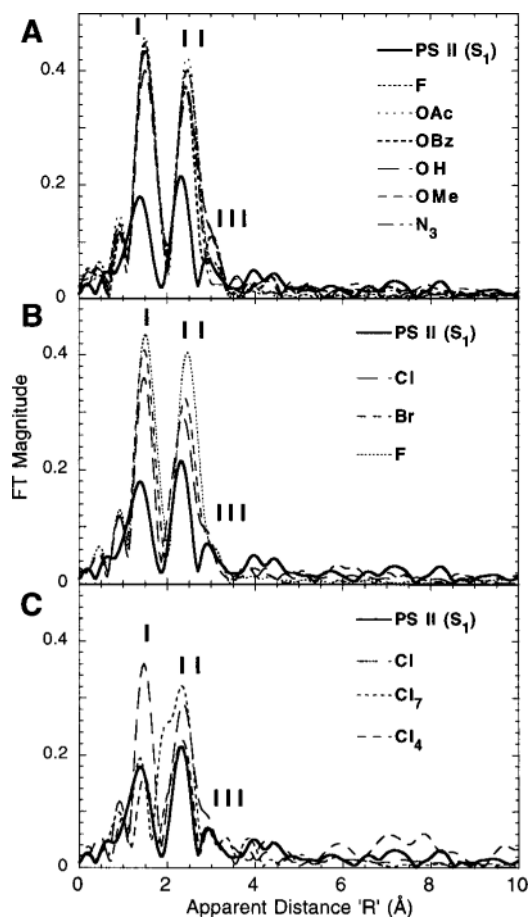
**Figure 6.**
Fourier transform spectra of raw *k*-space Mn EXAFS from PS II in the $S_1$ state and model compounds: (A) **OBz**, **OAc**, **OMe**, **OH, N$_3$**, and **F**; (B) **F**, **Cl**, and **Br**; (C) **Cl**, **Cl$_4$**, and **Cl$_7$**. The *k*-ranges used were the same as in Figure 4, and the minor peaks at $R' < 1$ Å are due to the residual background.
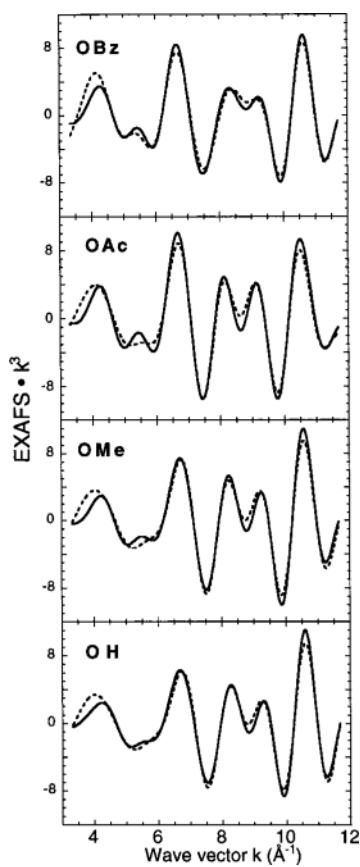
**Figure 7.**
Simulation (- - -) of Fourier transform peaks I, II, and III plotted over the Fourier-filtered *k*-space EXAFS (—) of **OBz**, **OAc**, **OMe**, and **OH**. Fits were generated as described in the text and Table 2 (fit labels 2, 3, 5, and 6, respectively).
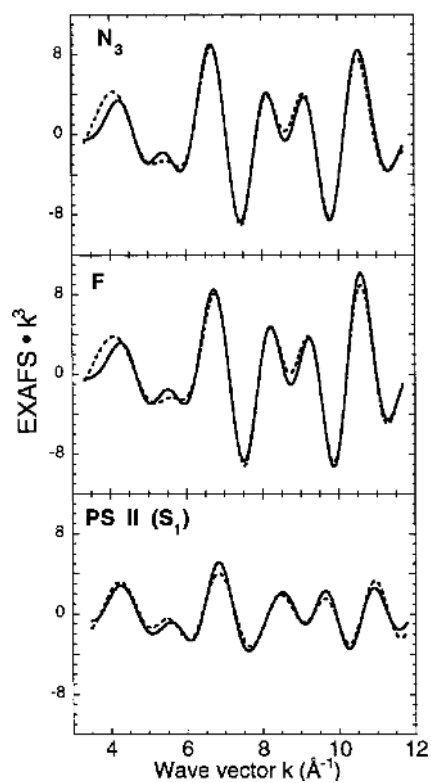
**Figure 8.**
Simulation (- - -) of Fourier transform peaks I, II, and III plotted over the Fourier-filtered *k*-space EXAFS (—) of **N₃**, **F** and PS II. Fits were generated as described in the text and Table 2 (fit labels 8, 9, and 15, respectively).
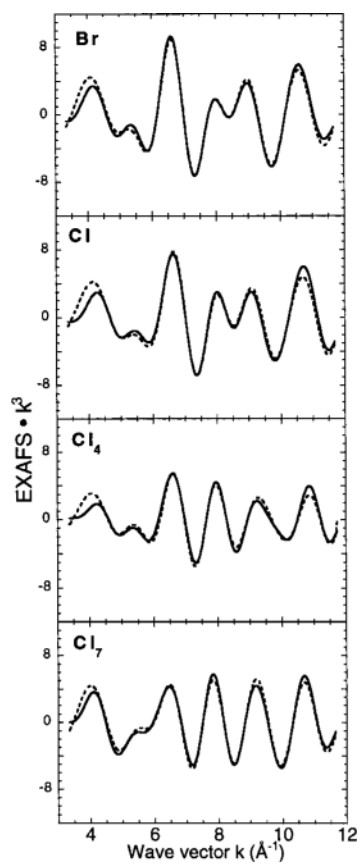
**Figure 9.**
Simulation (- - -) of Fourier transform peaks I, II, and III plotted over the Fourier-filtered *k*-space EXAFS (—) of **Cl**, **Br**, **Cl₄**, and **Cl₇**. Fits were generated as described in the text and Table 2 (fit labels 10, 11, 12, and 14, respectively).

**Table 1**

Mn K-Edge Rising Edge Inflection Point (Edge Position) and Mn–O Bond Length for Mn Model Compounds and Different S States of the OEC[a]

| compound | edge position (eV) | average Mn–O bond length (Å) (for O cubanes) | BVS | ref |
|---|---|---|---|---|
| PS II $S_0$ | 6550.1 | | | 18 |
| PS II $S_1$ | 6551.7 | | | 18 |
| PS II $S_2$ | 6553.5 | | | 18 |
| $Mn_4O_3$(**OBz**)(OBz)$_3$(dbm)$_3$ | 6550.9 | 1.932 | 3.20 | 51 |
| $Mn_4O_3$(**OAc**)(OAc)$_3$(dbm)$_3$ | 6551.5 | 1.919 | 3.17 | 46 |
| $Mn_4O_3$(**OMe**)(OAc)$_3$(dbm)$_3$ | 6551.3 | 1.919 | 3.21 | 47 |
| $Mn_4O_3$(**OH**)(OAc)$_3$(dbm)$_3$ | 6551.8 | 1.910 | 3.22 | 47 |
| $Mn_4O_3$(**N$_3$**)(OAc)$_3$(dbm)$_3$ | 6551.1 | | | 48 |
| $Mn_4O_3$**F**(OAc)$_3$(dbm)$_3$ | 6551.5 | | | 49 |
| $Mn_4O_3$**Cl**(OAc)$_3$(dbm)$_3$ | 6548.7 | | | 45, 50 |
| $Mn_4O_3$**Cl$_4$**(OAc)$_3$(py)$_3$ | 6548.5 | | | 49, 52 |
| [Hpy]$_3$$Mn_4O_3$**Cl$_7$**(OAc)$_3$ | 6548.4 | | | 45 |
| $Mn_4O_3$**Br**(OAc)$_3$(dbm)$_3$ | 6549.3 | | | 45 |

[a]The estimated error in the Mn K-edge positions (inflection points) is ±0.2 eV from previous XANES measurements on PS II.

**Table 2**

Least-Squares Best Fits of Filtered Peaks I, II, and (III) from the Mn Cubanes and PS II[a]

| compound | fit label | atom | $R$ (Å) | $N$ | $\sigma^2 \times 10^3$ | $\Delta E_0$ (eV) | $\Phi \times 10^3$ | $\varepsilon^2 \times 10^5$ | XRD $R$ (Å) | XRD $N$ |
|---|---|---|---|---|---|---|---|---|---|---|
| $Mn_4O_3(\mathbf{OBz})(OBz)_3(dbm)_3$ | 1 | O | 1.907 | 4.75 | 3 | −7 | 0.41 | 0.43 | 1.932 | 4.75 |
| | | Mn | 2.818 | 1.5 | 2 | | | | 2.790 | 1.5 |
| | | Mn | 3.160 | 0.5 | 2 | | | | 3.183 | 0.5 |
| | | Mn | 3.375 | 1.0 | 2 | | | | 3.370 | 1.0 |
| " | 2 | O | 1.911 | 4.75 | 3 | −7 | 0.24 | 0.30 | 1.932 | 4.75 |
| | | O | 2.198 | 1.25 | 2 | | | | 2.198 | 1.25 |
| | | Mn | 2.814 | 1.5 | 2 | | | | 2.790 | 1.5 |
| | | Mn | 3.169 | 0.5 | 2 | | | | 3.183 | 0.5 |
| | | Mn | 3.385 | 1.0 | 3 | | | | 3.370 | 1.0 |
| $Mn_4O_3(\mathbf{OAc})(OAc)_3(dbm)_3$ | 3 | O | 1.900 | 4.5 | 2 | −13 | 0.26 | 0.25 | 1.919 | 4.5 |
| | | O | 2.243 | 1.5 | 5 | | | | 2.228 | 1.5 |
| | | Mn | 2.805 | 1.5 | 2 | | | | 2.799 | 1.5 |
| | | Mn | 3.166 | 1.5 | 2 | | | | 3.201 | 1.5 |
| $Mn_4O_3(\mathbf{OMe})(OAc)_3(dbm)_3$ | 4 | O | 1.899 | 4.5 | 2 | −13 | 0.25 | 0.25 | 1.919 | 4.5 |
| | | O | 2.203 | 1.5 | 4 | | | | 2.194 | 1.5 |
| | | Mn | 2.800 | 1.5 | 2 | | | | 2.798 | 1.5 |
| | | Mn | 3.117 | 1.5 | 2 | | | | 3.132 | 1.5 |
| $Mn_4O_3(\mathbf{OH})(OAc)_3(dbm)_3$ | 5 | O | 1.903 | 4.5 | 3 | −13 | 0.22 | 0.20 | 1.910 | 4.5 |
| | | O | 2.191 | 1.5 | 2 | | | | 2.210 | 1.5 |
| | | Mn | 2.803 | 1.5 | 2 | | | | 2.789 | 1.5 |
| | | Mn | 3.083 | 1.5 | 2 | | | | 3.122 | 1.5 |
| $Mn_4O_3(\mathbf{N_3})(OAc)_3(dbm)_3$ | 6 | O | 1.901 | 4.5 | 2 | −13 | 0.19 | 0.17 | 1.910 | 4.5 |
| | | O(N) | 2.227 | 1.5 | 7 | | | | 2.239 | 1.5 |
| | | Mn | 2.807 | 1.5 | 2 | | | | 2.794 | 1.5 |
| | | Mn | 3.160 | 1.5 | 3 | | | | 3.189 | 1.5 |
| $Mn_4O_3\mathbf{F}(OAc)_3(dbm)_3$ | 7 | O | 1.896 | 4.5 | 2 | −13 | 0.20 | 0.19 | 1.913 | 4.5 |
| | | O(F) | 2.190 | 1.5 | 5 | | | | 2.196 | 1.5 |
| | | Mn | 2.794 | 1.5 | 2 | | | | 2.786 | 1.5 |

| compound | fit label | atom | $R$ (Å) | $N$ | $\sigma^2 \times 10^3$ | $\Delta E_0$ (eV) | $\Phi \times 10^3$ | $e^2 \times 10^5$ | XRD $R$ (Å) | XRD $N$ |
|---|---|---|---|---|---|---|---|---|---|---|
| Mn$_4$O$_3$Cl(OAc)$_3$(dbm)$_3$ | 9 | Mn | 3.122 | 1.5 | 4 | | | | 3.145 | 1.5 |
| | | O | 1.912 | 4.5 | 4 | −8 | 0.31 | 0.39 | 1.914 | 4.5 |
| | | O | 2.145 | 0.75 | 2 | | | | 2.165 | 0.75 |
| | | Cl | 2.606 | 0.75 | 2 | | | | 2.650 | 0.75 |
| | | Mn | 2.811 | 1.5 | 4 | | | | 2.795 | 1.5 |
| | | Mn | 3.244 | 1.5 | 5 | | | | 3.251 | 1.5 |
| Mn$_4$O$_3$Cl$_4$(OAc)$_3$(py)$_3$ | 10 | O | 1.873 | 3.0 | 10 | −15 | 0.38 | 0.41 | 1.926 | 3.0 |
| | | Cl | 2.215 | 0.75 | 6 | | | | 2.237 | 0.75 |
| | | Cl | 2.580 | 0.75 | 2 | | | | 2.627 | 0.75 |
| | | Mn | 2.774 | 1.5 | 4 | | | | 2.815 | 1.5 |
| | | Mn | 3.239 | 1.5 | 4 | | | | 3.269 | 1.5 |
| [Hpy]$_3$Mn$_4$O$_3$**Cl$_7$**(OAc)$_3$ | 11 | O | 1.916 | 3.0 | 7 | −11 | 0.17 | 0.18 | 1.933 | 3 |
| | | Cl | 2.277 | 1.5 | 3 | | | | 2.267 | 1.5 |
| | | Cl | 2.622 | 0.75 | 2 | | | | 2.634 | 0.75 |
| | | Mn | 2.823 | 1.5 | 3 | | | | 2.829 | 1.5 |
| | | Mn | 3.277 | 1.5 | 6 | | | | 3.302 | 1.5 |
| Mn$_4$O$_3$**Br**(OAc)$_3$(dbm)$_3$ | 12 | O | 1.905 | 4.5 | 3 | −10 | 0.17 | 0.21 | 1.914 | 4.5 |
| | | O | 2.196 | 0.75 | 3 | | | | 2.163 | 0.75 |
| | | Br | 2.698 | 0.75 | 3 | | | | 2.803 | 0.75 |
| | | Mn | 2.859 | 1.5 | 2 | | | | 2.794 | 1.5 |
| | | Mn | 3.272 | 1.5 | 5 | | | | 3.282 | 1.5 |
| PS II (S$_1$ state) | 13 | O | 1.859 | 2.5 | 6 | −14 | 0.35 | 0.25 | | |
| | | Mn | 2.731 | 1.0 | 2 | | | | | |
| | | Mn | 3.308 | 0.5 | 4 | | | | | |

[a]For the model compounds EXAFS results are compared to interatomic distances reported from X-ray diffraction data (XRD $N$; see references in Table 1). $N$ is fixed to known values from XRD data. Fit parameters are as defined in the text, with $S_0^2 = 0.85$ in all fits.

**Table 3**

Least-Squares Best Fits of Filtered Peak II for the "O" Cubanes and PS II[a]

| compound | fit label | atom | $R$ (Å) | N | $\sigma^2 \times 10^3$ | $\Delta E_0$ (eV) | $\Phi \times 10^3$ | $\varepsilon^2 \times 10^5$ | XRD $N$ |
|---|---|---|---|---|---|---|---|---|---|
| $Mn_4O_3(\mathbf{OBz})(OBz)_3(dbm)_3$ | 14 | Mn | 2.841 | 1.9 | 1 | −1 | 0.165 | 2000 | 1.5 |
| | | Mn | 3.012 | 0.33 | 2 | | | | 0.5 |
| | | Mn | 3.412 | 1.1 | 6 | | | | 1.0 |
| " | 15 | Mn | 2.831 | 1.7 | 1 | −3 | 0.15 | 0.24 | 1.5 |
| | | Mn | 3.410 | 1.3 | 7 | | | | 1.5 |
| $Mn_4O_3(\mathbf{OAc})(OAc)_3(dbm)_3$ | 16 | Mn | 2.818 | 1.8 | 1 | −9 | 0.14 | 0.28 | 1.5 |
| | | Mn | 3.193 | 1.4 | 2 | | | | 1.5 |
| $Mn_4O_3(\mathbf{OMe})(OAc)_3(dbm)_3$ | 17 | Mn | 2.829 | 1.8 | 1 | −5 | 0.20 | 0.45 | 1.5 |
| | | Mn | 3.138 | 1.0 | 2 | | | | 1.5 |
| $Mn_4O_3(\mathbf{OH})(OAc)_3(dbm)_3$ | 18 | Mn | 2.787 | 1.2 | 1 | −20 | 0.22 | 0.36 | 1.5 |
| | | Mn | 3.057 | 1.7 | 1 | | | | 1.5 |
| $Mn_4O_3(\mathbf{N_3})(OAc)_3(dbm)_3$ | 19 | Mn | 2.811 | 1.5 | 1 | −11 | 0.15 | 0.20 | 1.5 |
| | | Mn | 3.179 | 1.4 | 3 | | | | 1.5 |
| $Mn_4O_3\mathbf{F}(OAc)_3(dbm)_3$ | 20 | Mn | 2.777 | 1.4 | 1 | −20 | 0.19 | 0.36 | 1.5 |
| | | Mn | 3.123 | 1.3 | 1 | | | | 1.5 |
| PS II ($S_1$ state) | 21 | Mn | 2.744 | 1.3 | 3 | −11 | 0.18 | 0.26 | |
| | | Mn | 3.320 | 0.6 | 4 | | | | |

[a]For the "O" cubanes, Mn EXAFS results are compared to coordination numbers reported from X-ray diffraction data (XRD $N$; see references in Table 1). $N$ is allowed to float in these fits, and is not fixed as in Table 2. Fit parameters are as defined in the text. $S_0^2 = 0.85$ in all fits.